Journal of Computational Applied Mechanics 2026, 57(2): 195-211

DOI: 10.22059/jcamech.2025.406512.1698

RESEARCH PAPER

# Unsteady Fractional MHD Flow of Blood-Based Au-Cu Hybrid Nanofluids: Coupled Heat-Mass Transfer with Dufour-Soret Effects and Biomedical Implications

Ji-Huan He [a, *], M. Y Adamu [b], Isah Abdullahi [b], Nuo Xu [c], Chun-Hui He [d, †]

[a] *School of Information Engineering, Yango University, Fuzhou, China*
[b] *Department of Mathematics Abubakar Tafawa Balewa University Bauchi, Nigeria*
[c] *School of Civil Engineering and Transportation, South China University of Technology, Guangzhou 510641, China*
[d] *School of Civil Engineering & Transportation, Foshan University, Foshan 528000, China*

**Abstract**

**This study investigates the unsteady magnetohydrodynamic (MHD) flow of blood-based Au-Cu hybrid nanofluids in cylindrical arteries, integrating thermal radiation, Joule heating, chemical reactions, and Dufour-Soret cross-diffusion effects. These effects are critical for biomedical applications like hyperthermia and targeted drug delivery. A Caputo time-fractional derivative is adopted to capture memory-dependent behaviors of biological fluids, which are typically overlooked by classical models. The governing equations for velocity, temperature, and nanoparticle concentration are transformed via Laplace transforms and solved semi-analytically using the Concentrated Matrix Exponential method. This ensures accuracy and computational efficiency. The results indicate that increasing the fractional-order parameter delays momentum, thermal, and concentration diffusion, thereby reflecting stronger memory effects. Magnetic fields have been shown to reduce velocity but enhance temperature via Joule heating. Furthermore, higher Dufour numbers have been demonstrated to strengthen temperature gradients, while elevated Soret numbers have been shown to intensify concentration gradients. This article's novelty lies in its integration of fractional calculus with hybrid nanofluid MHD modeling, accounting for complex coupled effects. The proposed model provides more realistic predictions of unsteady biological flows, offering valuable insights for optimizing biomedical therapies and cardiovascular device design.**

**Keywords:** Hybrid nanofluid flow; Fractional-order model; MHD; Dufour and Soret effects; Thermal radiation; Chemical reaction; Arterial flow; Biomedical applications.

## 1. Introduction

Hybrid nanofluids [1], composed of multiple types of nanoparticles suspended in biological fluids, have emerged as a promising frontier in biomedical engineering, particularly for enhancing drug delivery, thermal management and targeted therapies in cardiovascular systems. Recent studies have indicated that the incorporation of

* Corresponding author. *E-mail address:* hejihuan@ygu.edu.cn
† Corresponding author. *E-mail address:* mathew_he@yahoo.com

nanoparticles, including gold (Au), copper (Cu), silver (Ag), and carbon nanotubes into blood significantly alters its rheological and transport properties, thereby creating opportunities for advancements in drug delivery, medical imaging, and targeted hyperthermi [2]. Magnetohydrodynamic (MHD) systems [3], which utilize external magnetic fields to manipulate these nanofluids, offer significant advantages. First, the external magnetic fields can guide nanoparticles to specific target sites (e.g., tumors or blocked arteries).

It is important to note that thermal radiation and thermo-solutal cross-diffusion effects specifically the Dufour (heat transfer induced by concentration gradients) and Soret (mass transfer induced by temperature gradients) phenomena play critical roles in regulating nanoparticle migration and drug concentration distributions, directly impacting therapeutic efficacy. Furthermore, chemical reactions in the bloodstream (e.g., those arising from metabolic processes or the introduction of therapeutic agents) further complicate flow dynamics by altering fluid properties and nanoparticle-tissue interactions. A critical aspect of enhancing the efficacy of nanoparticle-mediated therapies is to investigate the interplay between these reactions and the effects of cross-diffusion [4]. This is a key finding highlighted in recent studies on Casson fluid-based hybrid nanoflows in inclined arteries [5].

It has been demonstrated that the Dufour and Soret effects significantly enhance heat and mass transfer in nanofluid flows, underscoring their significance in biomedical applications [6].

The efficacy of fractional calculus, particularly the Caputo derivative, in modeling MHD blood flows within complex arterial structures, such as stenosed or inclined arteries, has been demonstrated. The incorporation of factors such as Joule heating, thermal radiation, and variable viscosity has been demonstrated to yield results that exhibit a stronger correlation with experimental data [7]. The capacity to capture memory-dependent behaviors and non-local interactions renders fractional-order models more efficacious than conventional integer-order ones when simulating biological fluids. Furthermore, the findings of Yakubu et al. [8] demonstrated that fractional-order solutions provide more precise descriptions of velocity, temperature, and concentration profiles in comparison to integer-order models.

However, there are critical gaps in the existing body of knowledge. More research is needed to elucidate the interplay between viscous dissipation, Joule heating, radiation, and cross-diffusion effects in blood-based hybrid nanofluids. However, existing studies often overlook the significance of internal heating mechanisms, such as viscous and electromagnetic effects, in physiological flows. For instance, Joule heating under MRI conditions can lead to local temperature elevations, while viscous dissipation drives energy generation in micro vessels. The integration of these mechanisms with Dufour, Soret, radiation, and chemical reactions is imperative for the development of realistic models in domains such as nanoparticle-based drug delivery and hyperthermia.

Furthermore, extant models seldom incorporate radiation, chemical reactions, Dufour-Soret effects, and Caputo fractional dynamics in Au-Cu blood-based hybrid nanofluids [9]. In response to this limitation, this study explores how these phenomena interact to improve knowledge of hybrid nanofluid dynamics in arterial systems, with relevance to controlled drug transport, magnetic heat therapy, and the management of cardiovascular circulation.

## 2. Formulation of the Problem

### *2.1 Flow Geometry*

A mathematical model is used to study the MHD flow of a blood-based hybrid nanofluid in a vessel, which, as seen in Figure 1, is idealized as a one-dimensional cylindrical tube of constant radius ($R_0$) and smooth walls. The present study focuses on two types of nanoparticles: gold (Au) and copper (Cu). These were selected for their well-documented roles in blood transport, targeted drug delivery, and the treatment of cardiovascular conditions like hypertension [10]. The nanoparticles are assumed to be uniformly dispersed in the blood and in thermal equilibrium with the fluid. The axisymmetric flow moves axially with velocity ($u_z$) under a uniform transverse magnetic field ($B_0$), and the vessel wall is maintained at a constant core-body temperature.

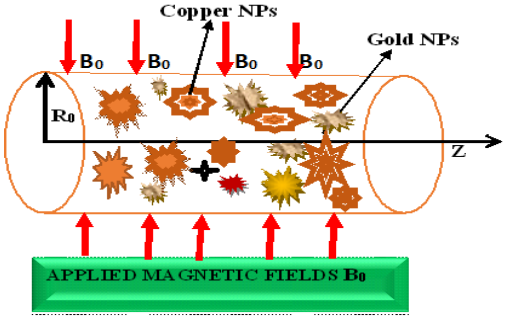

**Fig. 1. Magnetohydrodynamic (MHD) Flow of Au-Cu Hybrid Nanofluid in a Cylindrical Artery.**

*2.2 Basic flow equations of the given problem*

In line with the methodology in [9], the governing equations for arterial blood flow, comprising the momentum, energy, and nanoparticle concentration equations in cylindrical coordinates, are as follows:

$$\left.\begin{aligned}\rho_{hnf}\frac{\partial \hat{u}_z}{\partial \hat{t}} = -\frac{\partial \hat{p}}{\partial \hat{z}} + \mu_{hnf}\left(\frac{\partial^2 \hat{u}_z}{\partial \hat{r}^2} + \frac{1}{\hat{r}}\frac{\partial \hat{u}_z}{\partial \hat{r}}\right) - \sigma_{hnf}B_0^2\hat{u}_z - \frac{\mu_{hnf}}{K}\hat{u}_z \\ g\beta_T(\rho\alpha_T)_{hnf}(\hat{T}-\hat{T}_w) + g\beta_C(\rho\alpha_C)_{hnf}(\hat{C}-\hat{C}_w)\end{aligned}\right\} \tag{1}$$

$$(\rho C_p)_{hnf}\frac{\partial \hat{T}}{\partial \hat{t}} = k_{hnf}\left(\frac{\partial^2 \hat{T}}{\partial \hat{r}^2} + \frac{1}{\hat{r}}\frac{\partial \hat{T}}{\partial \hat{r}}\right) + Q_u + Q_B - \frac{\partial q}{\partial \hat{r}} + \frac{D_m K_T}{C_S}\left(\frac{\partial^2 \hat{C}}{\partial \hat{r}^2} + \frac{1}{\hat{r}}\frac{\partial \hat{C}}{\partial \hat{r}}\right) \tag{2}$$

$$\frac{\partial \hat{C}}{\partial \hat{t}} = D_{hnf}\left(\frac{\partial^2 \hat{C}}{\partial \hat{r}^2} + \frac{1}{\hat{r}}\frac{\partial \hat{C}}{\partial \hat{r}}\right) - A(\hat{C}-\hat{C}_w) + \frac{D_m K_T}{T_\infty}\left(\frac{\partial^2 \hat{T}}{\partial \hat{r}^2} + \frac{1}{\hat{r}}\frac{\partial \hat{T}}{\partial \hat{r}}\right) \tag{3}$$

The equations for thermal radiation and pressure gradient in a vibrational environment were provided in [8]; respectively

$$-\frac{\partial \hat{p}}{\partial \hat{z}} = \hat{a}_0 + \hat{a}_1\cos(\hat{\omega}\hat{t}) \tag{4}$$

$$-\frac{\partial q}{\partial \hat{r}} = 4\alpha^2\left(\hat{T}-\hat{T}_w\right) \tag{5}$$

The mathematical expressions for thermal radiation and pressure gradient under vibrational circumstances are cited from [11]. In this context, key thermophysical properties of the hybrid nanofluid are taken into account, including dynamic viscosity ($\mu_{nf}$), thermal expansion coefficient ($\beta$), thermal conductivity ($k_{nf}$), and specific heat capacity ($Cp)_{nf}$). Moreover, essential energy-related terms such as viscous dissipation ($Q_v$), Joule heating ($Q_f$), and thermal radiation ($Q_r = \mu_0 H_0^2(\partial^2 u_z/\partial t^2)$) are integrated, along with the magnetic parameter ($\theta_\beta = \sigma B_0^2/\mu_0$), to accurately capture the dynamic characteristics of the flow system. Corresponding initial and boundary conditions are applied to address the specific physical constraints of the problem.

The initial and boundary conditions are given below:

$$\left.\begin{aligned}&\hat{u}_z = \hat{u}_{z0}, \hat{T} = \hat{T}_0, \hat{C} = \hat{C}_0; && \forall \hat{r} \in (0.R_0), && at && \hat{t} = 0 \\ &\frac{\partial \hat{u}_z}{\partial \hat{r}} = 0, \frac{\partial \hat{T}}{\partial \hat{r}} = 0, \frac{\partial \hat{C}}{\partial \hat{r}} = 0; && \forall t > 0, && at && \hat{r} = 0 \\ &\hat{u}_z = 0, \hat{T} = \hat{T}_w, \hat{C} = \hat{C}_0; && \forall \hat{t} > 0 && at && \hat{r} = R_0\end{aligned}\right\} \tag{6}$$

Here, $\hat{u}_{z0}$ corresponds to the reference speed, $\hat{T}_0$ denotes the initial temperature, and $\hat{C}_0$ represents the initial concentration (i.e., nanoparticle distribution).

## 3. Theory development

The problem is addressed by defining suitable dimensionless variables, which are used to convert Equations (1) to (3) into their non-dimensional forms through the process of non-dimensionalization.

$$r=\frac{\hat{r}}{R_0},z=\frac{\hat{z}}{R_0},t=\frac{u_{z0}\hat{t}}{R_0},u_z=\frac{\hat{u}_z}{u_{z0}},p=\frac{\hat{p}}{\rho u_{z0}^2},$$
$$\theta=\frac{\hat{T}-\hat{T}_w}{\hat{T}_w-\hat{T}_\infty},k=\frac{\hat{k}R_0}{u_{z0}},\varphi=\frac{\hat{C}-\hat{C}_w}{\hat{C}_w-\hat{C}_\infty} \tag{7}$$

By substituting Eqs. (4) and (5) into the governing equations, and incorporating the dimensionless parameters defined in Eq. (7), the model equations and their corresponding boundary conditions are transformed into the following dimensionless forms after omitting the overbars for simplicity.

$$\left.\begin{aligned} &b_1\frac{\partial u_z(r,t)}{\partial t}=a_0+a_1\cos(\omega t)+\frac{b_2}{R_e}\left[\frac{\partial^2 u_z(r,t))}{\partial r^2}+\frac{1}{r}\frac{\partial u_z(r,t)}{\partial r}\right]\\ &-\frac{b_3}{R_e}Ha^2u_z(r,t)+\frac{b_4}{R_e}Gr\theta(r,t)+\frac{b_5}{R_e}Gc\varphi(r,t)-\frac{b_2}{DaR_e}u(r,t)\end{aligned}\right\} \tag{8}$$

$$\left.\begin{aligned} &b_6\frac{\partial\theta(r,t)}{\partial t}=\frac{b_7}{P_e}\left[\frac{\partial^2\theta(r,t)}{\partial r^2}+\frac{1}{r}\frac{\partial\theta(r,t)}{\partial r}\right]+R\theta(r,t)+\frac{b_2Ec}{R_e}\left(\frac{\partial u_z(r,t)}{\partial r}\right)^2+\\ &\frac{b_3EcHa^2}{R_e}u_z^2+D_f\left(\frac{\partial^2\varphi(r,t)}{\partial r^2}+\frac{1}{r}\frac{\partial\varphi(r,t)}{\partial r}\right)\end{aligned}\right\} \tag{9}$$

$$Sc\,\mathrm{Re}\frac{\partial\varphi}{\partial t}=b_8\left[\frac{\partial^2\varphi(r,t)}{\partial r^2}+\frac{1}{r}\frac{\partial\varphi(r,t)}{\partial r}\right]-C_rSc\,\mathrm{Re}^2\,\varphi(r,t)+Sr\left[\frac{\partial^2\theta(r,t)}{\partial r^2}+\frac{1}{r}\frac{\partial\theta(r,t)}{\partial r}\right] \tag{10}$$

Consequently, Eq.(6) becomes

$$\left.\begin{aligned} &u_z=u_{z0},\theta=\theta_0,\varphi=\varphi_0; && \forall\hat{r}\in(0,1), && at && t=0\\ &\frac{\partial u_z}{\partial r}=0,\frac{\partial\theta}{\partial r}=0,\frac{\partial\varphi}{\partial r}=0; && \forall t>0, && at && r=0\\ &u_z=\vartheta,\theta=\theta_w,\varphi=0; && \forall t>0 && at && r=1\end{aligned}\right\} \tag{11}$$

Hartman Number, Prandtl number, Grashof thermal number, Soret number, Chemical reaction parameter, Grashof mass number, Smidt number, Dufour number, Reynolds number, Darcy number, thermal radiation parameter, Peclet number and Eckert number are defined respectively as

$$Ha^2=\frac{\sigma_f B_0^2R_0}{\mu_f},\mathrm{Pr}=\frac{\mu_fC_p}{k_f},Gr=\frac{\rho_f(\alpha_T)_f g(T-T_\infty)R_0^2}{\mu_fu_{z0}},S_r=\frac{D_mK_T(T-T_\infty)}{\nu T_\infty(C-C_\infty)},Cr=\frac{A\nu}{u_{z0}^2},Gc=\frac{\rho_f(\alpha_T)_f g(C-C_\infty)R_0^2}{\mu_fu_{z0}},$$
$$Sc=\frac{\nu}{D_m},D_f=\frac{D_mK_T(C-C_\infty)}{C_sC_\rho(T-T_\infty)},\mathrm{Re}=\frac{R_0u_{z0}}{\nu},Da=\frac{k_p}{R_0^2},R=\frac{4\alpha_1^2R_0^2}{k},Pe=\mathrm{Re}.\mathrm{Pr},Ec=\frac{u_{z0}^2}{C_p(T-T_\infty)}$$

The coefficients $b_i$ are defined as ;

$$b_1=\frac{(\rho C_p)_{hnf}}{(\rho C_p)_f},b_2=\frac{k_{hnf}}{k_f},b_3=\frac{(\rho)_{hnf}}{(\rho)_f},b_4=\frac{\mu_{hnf}}{\mu_f},b_5=\frac{(\rho\alpha_T)_{hnf}}{(\rho\alpha_T)_f},b_6=\frac{\sigma_{hnf}}{\sigma_f},b_7=\frac{(\rho\alpha_C)_{hnf}}{(\rho\alpha_C)_f},b_8=\frac{D_{hnf}}{D_f}$$

The initial and boundary conditions described in equation (11) represent a realistic physiological scenario of blood flow in an artery. Initially, the blood and nanoparticles are at rest, uniformly distributed, and at the body's core temperature. Along the centreline of the artery, symmetry is maintained, implying there is no variation in velocity, temperature, or nanoparticle concentration across this line. At the arterial wall, the no-slip condition ensures the blood adheres to the wall, while the wall temperature is kept constant at a lower reference level, and the concentration of nanoparticles at the wall is assumed to be zero, modeling possible absorption or chemical reactions.

These conditions are necessary to accurately capture how heat, mass, and momentum propagate within the artery over time under the influence of magnetic, thermal, and solutal effects.

**Table 1. Thermal and physical properties of nanoparticles and base fluid**

| Blood | Gold (Au) | Copper (Cu) | Physical properties |
|---|---|---|---|
| 1630 | 19320 | 8933 | $\rho(kgm^{-3})$ |
| 0.492 | 314 | 401 | $k(W(mK)^{-1})$ |
| 1.8 | 14 | 16.7 | $\alpha_T \times 10^{-6}(K^{-1})$ |
| 3594 | 129 | 385 | $C_P(J(kgK)^{-1})$ |
| $6.67 \times 10^{-1}$ | $4.1 \times 10^{-7}$ | $5.9.6 \times 10^{-7}$ | $\sigma((S.m)^{-1})$ |

*3.1 Fractional-Time Derivatives of Modeled Equations*

Fractional-order models have been demonstrated to enhance the precision with which spatial diffusion processes and memory-dependent behaviors are represented, thereby rendering them especially advantageous for the analysis of intricate biological systems. The application of fractional calculus in simulating non-Newtonian blood flow has also been well-supported; for example, Alhachami et al. [12] investigated time-fractional MHD flow over a flat plate, further substantiating the efficacy of fractional derivatives in blood flow modeling. The collective analysis of these studies substantiates the pivotal role of fractional-time derivatives in accurately delineating the intricate dynamics of biological fluids. Accordingly, the Caputo fractional derivative is employed in the transient terms of Equations (8)–(10) to derive the modified governing equations.

$$\left.\begin{aligned} b_1 D_t^{\alpha} u_z(r,t)) = a_0 + a_1\cos(\omega t) + \frac{b_2}{R_e}\left[\frac{\partial^2 u_z(r,t))}{\partial r^2} + \frac{1}{r}\frac{\partial u_z(r,t)}{\partial r}\right] \\ -\frac{b_3}{R_e}Ha^2 u_z(r,t) + \frac{b_4}{R_e}Gr\theta(r,t) + \frac{b_5}{R_e}Gc\varphi(r,t) - \frac{b_2}{DaR_e}u(r,t) \end{aligned}\right\} \tag{12}$$

$$\left.\begin{aligned} b_6 D_t^{\alpha}\theta(r,t) = \frac{b_7}{P_e}\left[\frac{\partial^2\theta(r,t)}{\partial r^2} + \frac{1}{r}\frac{\partial\theta(r,t)}{\partial r}\right] + R\theta(r,t) + \frac{b_2 Ec}{R_e}\left(\frac{\partial u_z(r,t)}{\partial r}\right)^2 + \\ \frac{b_3 EcHa^2}{R_e}u_z^2 + D_f\left(\frac{\partial^2\varphi(r,t)}{\partial r^2} + \frac{1}{r}\frac{\partial\varphi(r,t)}{\partial r}\right) \end{aligned}\right\} \tag{13}$$

$$Sc\,\mathrm{Re}\,D_t^{\alpha}\varphi(r,t) = b_8\left[\frac{\partial^2\varphi(r,t)}{\partial r^2} + \frac{1}{r}\frac{\partial\varphi(r,t)}{\partial r}\right] - C_r Sc\,\mathrm{Re}^2\,\varphi(r,t) + Sr\left[\frac{\partial^2\theta(r,t)}{\partial r^2} + \frac{1}{r}\frac{\partial\theta(r,t)}{\partial r}\right] \tag{14}$$

The Caputo fractional operator is defined as [30]

$$D_t^{\alpha}u(r,t) = \frac{1}{\Gamma(1-\alpha)}\int_0^t (t-\tau)^{-\alpha}u'(\tau)d\tau$$

*3.2 Analytical solutions*

In this study, the governing equations for hybrid nanofluid flow are addressed using a combination of the Concentrated Matrix-Exponential (CME) method and the Laplace transform technique. The efficacy of these methods in managing transient terms and system nonlinearities is well-documented, enabling the development of a semi-analytical solution that maintains a balance between computational precision and efficiency. As demonstrated in previous studies, the incorporation of fractional calculus has been shown to enhance the model's capacity to accurately capture the complex behavior of blood flow in stenosed arteries [13].

The semi-analytical solution to the governing equations commences with the transformation of the transient terms, subsequently accompanied by the incorporation of explicit elementary factors. Collectively, these factors metamorphose the equations into their modified forms, as depicted in Equations (15) through (17).

$$\left.\begin{aligned} b_1\left(s^{\alpha}\bar{u}_z(r,s)-\sum_{m=0}^{n-1}s^{\alpha-1-m}\bar{u}_z(r,0)\right)&=\left(\frac{a_0}{s}+a_1\frac{s}{s^2+\omega^2}\right)+\frac{b_2}{R_e}\left[\frac{\partial^2\bar{u}_z(r,s))}{\partial r^2}+\frac{1}{r}\frac{\partial\bar{u}_z(r,s)}{\partial r}\right]\\ -\frac{b_3}{R_e}Ha^2\bar{u}_z(r,s)+\frac{b_4}{R_e}Gr\bar{\theta}(r,s)+\frac{b_5}{R_e}Gc\bar{\varphi}(r,s)-\frac{b_2}{DaR_e}\bar{u}_z(r,s)&\end{aligned}\right\} \tag{15}$$

$$\left.\begin{aligned} b_6\left(s^{\alpha}\bar{\theta}(r,s)-\sum_{m=0}^{n-1}s^{\alpha-1-m}\bar{\theta}(r,0)\right)&=\frac{b_7}{P_e}\left[\frac{\partial^2\bar{\theta}(r,s)}{\partial r^2}+\frac{1}{r}\frac{\partial\bar{\theta}(r,s)}{\partial r}\right]+\\ R\bar{\theta}(r,t)+\frac{b_2Ec}{R_e}\left(\frac{\partial\bar{u}_z(r,s)}{\partial r}\right)^2+\frac{b_3EcHa^2}{R_e}\bar{u}_z^2+D_f\left(\frac{\partial^2\bar{\varphi}(r,s)}{\partial r^2}+\frac{1}{r}\frac{\partial\bar{\varphi}(r,s)}{\partial r}\right)&\end{aligned}\right\} \tag{16}$$

$$\left.\begin{aligned} Sc\,\mathrm{Re}\left(s^{\alpha}\bar{\varphi}(r,s)-\sum_{m=0}^{n-1}s^{\alpha-1-m}\bar{\varphi}(r,0)\right)&=b_8\left[\frac{\partial^2\bar{\varphi}(r,s)}{\partial r^2}+\frac{1}{r}\frac{\partial\bar{\varphi}(r,s)}{\partial r}\right]-\\ C_r Sc\,\mathrm{Re}^2\,\bar{\varphi}(r,s)+Sr\left[\frac{\partial^2\bar{\theta}(r,s)}{\partial r^2}+\frac{1}{r}\frac{\partial\bar{\theta}(r,s)}{\partial r}\right]&\end{aligned}\right\} \tag{17}$$

Where $s^{\alpha}u(r,s)-\sum_{m=0}^{n-1}s^{\alpha-1-m}u^k(0)=0$.

Represents the Laplace transform of the Caputo fractional derivative. Additionally, the Laplace transforms of the associated boundary conditions are derived as follows:

$$\left.\begin{aligned} &\frac{\partial\bar{u}_z}{\partial r}=0,\frac{\partial\bar{\theta}}{\partial r}=0,\frac{\partial\bar{\varphi}}{\partial r}=0; \quad \forall t>0, \qquad at \qquad r=0\\ &\bar{u}_z=\frac{\vartheta}{s},\theta=\frac{\theta_w}{s},\varphi=0; \qquad \forall t>0 \qquad at \qquad r=1\end{aligned}\right\} \tag{18}$$

*3.2.1. Velocity profile*

To resolve the transformed momentum equation, we first implement the initial condition, $u_z(r,0) = u_{z0}(1-r^2)$, together with the constraints n = 1 and k = 0 into Eq.15, thus simplifying it to:

$$\left.\begin{aligned} &\left[\frac{d^2\bar{u}_z(r,s)}{dr^2}+\frac{1}{r}\frac{d\bar{u}_z(r,s)}{dr}\right]-\left(R_eb_9s^{\alpha}+b_{10}Ha^2+\frac{1}{Da}\right)\bar{u}_z(r,s)=\\ &-b_{11}\left(\frac{a_0}{s}+a_1\frac{s}{s^2+\omega^2}\right)R_e-b_{12}Gr\bar{\theta}(r,s)-b_{13}Gc\bar{\varphi}(r,s)-R_eb_9s^{\alpha-1-m}\bar{u}_{z0}(1-r^2)\end{aligned}\right\} \tag{19}$$

$$b_9=\frac{b_1}{b_2},b_{10}=\frac{b_3}{b_2},b_{11}=\frac{1}{b_2},b_{12}=\frac{b_4}{b_2},\quad b_{13}=\frac{b_5}{b_2},\ Q_{u2}=\left(R_eb_9s^{\alpha}+b_{10}Ha^2+\frac{1}{Da}\right)$$

$$P_{u2}=-b_{11}\left(\frac{a_0}{s}+a_1\frac{s}{s^2+\omega^2}\right)R_e-b_{12}Gr\bar{\theta}(r,s)-b_{13}Gc\bar{\varphi}(r,s)-R_eb_9s^{\alpha-1-m}\bar{u}_{z0}(1-r^2)$$

Eq.19, reduces to

$$\frac{d^2\bar{u}_z(r,s)}{dr^2}+\frac{1}{r}\frac{d\bar{u}_z(r,s)}{dr}-Qu_2\bar{u}_z(r,s)=Pu_2 \tag{20}$$

The homogeneous component of Eq. (20), which corresponds to the form of a modified Bessel equation, is solved initially to derive the corresponding complementary solution:

$$\overline{u}_z(r,s) = c_1 I_0(r\sqrt{Q_{u2}}) + c_2 K_0(r\sqrt{Q_{u2}}) \tag{21}$$

where $c_1$ and $c_2$ denote constants, $I_0$ and $K_0$ represent modified Bessel functions of the first and second kind, respectively. By employing the method of undetermined coefficients, we further obtain the particular solution for equation (21) as presented below:

$$\overline{u}_{zp} = \frac{P_{u2}}{Q_{u2}} \tag{22}$$

Adding Eqs. (21) and (22), and according to the boundary condition $d\overline{u}_z / dr(0) = 0$, the general solution of Eq. (20) is obtained as:

$$\overline{u}_z(r,s) = c_1 I_0(r\sqrt{Q_{u2}}) + c_2 K_0(r\sqrt{Q_{u2}}) - \frac{P_{u2}}{Q_{u2}} \tag{23}$$

So $I_0'(0)$ and $K_0'(0)$ in (23) can be calculated. However, $K_0'(0) \to \infty$, hence we set $c_2$=0, as a result, Eq.(23) becomes

$$\overline{u}_z(r,s) = c_1 I_0(r\sqrt{Q_{u2}}) - \frac{P_{u2}}{Q_{u2}} \tag{24}$$

Considering the boundary condition at $r$ = 1, we have

$$c_1 = \frac{1}{I_0\sqrt{Q_{u2}}}\left(\frac{\vartheta}{s} + \frac{P_{u2}(1,s)}{Q_{u2}}\right) \tag{25}$$

$$P_{u2}(1,s) = -b_{11}\left(\frac{a_0}{s} + a_1\frac{s}{s^2+\omega^2}\right)R_e - b_{12}Gr\overline{\theta}(1,s) - b_{13}Gc\overline{\varphi}(1,s) - R_e b_9 s^{\alpha-1-m}\overline{u}_{z0}(1-r^2)$$

Substituting Eq.25 in Eq.24, we obtain the solution of the velocity profile as;

$$\overline{u}_z(r,s) = \left(\frac{\vartheta}{s} + \frac{P_{u2}(1,s)}{Q_{u2}}\right)\frac{I_0(r\sqrt{Q_{u2}})}{I_0\sqrt{Q_{u2}}} - \frac{P_{u2}}{Q_{u2}} \tag{26}$$

Replacing the values of $Q_{u2}$ , $P_{u2}(1,s)$ and $P_{u2}$ in Eq. (26), simplifying it, we have the general solution of the momentum equation in the Laplace domain as;

$$\begin{aligned}
&\overline{u}_z(r,s) = \left\{\left(\frac{\vartheta}{s} + \Pi_1\right)\Pi_2 + \Pi_3\right\} \\
&\Pi_1 = \frac{-b_{11}\left(\frac{a_0}{s} + a_1\frac{s}{s^2+\omega^2}\right)R_e - b_{12}Gr\overline{\theta}_0(1,s) - b_{13}Gc\overline{\varphi}_0(1,s) - R_e b_9 s^{\alpha-1-m}\overline{u}_{z0}(1-r^2)}{R_e b_9 s^{\alpha} + b_{10}Ha^2 + 1/Da} \\
&\Pi_2 = \frac{I_0\left(r\sqrt{(R_e b_9 s^{\alpha} + b_{10}Ha^2 + 1/Da)}\right)}{I_0\left(\sqrt{(R_e b_9 s^{\alpha} + b_{10}Ha^2 + 1/Da)}\right)} \\
&\Pi_3 = \frac{b_{11}\left(\frac{a_0}{s} + a_1\frac{s}{s^2+\omega^2}\right)R_e + b_{12}Gr\overline{\theta}(r,s) + b_{13}Gc\overline{\varphi}(r,s) + R_e b_9 s^{\alpha-1-m}\overline{u}_{z0}(1-r^2)}{(R_e b_9 s^{\alpha} + b_{10}Ha^2 + 1/Da)}
\end{aligned} \tag{27}$$

*3.2.2. Temperature profile*

In a similar manner, Eq. (27) is reorganized and expressed in the following form:

$$\left.\begin{aligned}&\left[\frac{d^2\bar{\theta}(r,s)}{dr^2}+\frac{1}{r}\frac{d\bar{\theta}(r,s)}{dr}\right]+(b_{14}P_eR-b_{15}P_es^{\alpha})\bar{\theta}(r,s)=P_eb_{15}s^{\alpha-1}\theta_0\\&-b_{16}A_{18}Ec\,\mathrm{Pr}\left(\frac{d\bar{u}_z(r,s)}{dr}\right)^2-b_{17}EcHa^2\,\mathrm{Pr}(\bar{u}_z(r,s))^2-D_f\left(\frac{d^2\bar{\varphi}(r,s)}{dr^2}+\frac{1}{r}\frac{d\bar{\varphi}(r,s)}{dr}\right)\end{aligned}\right\} \tag{28}$$

$$b_{14}=\frac{1}{b_7},b_{15}=\frac{b_6}{b_7},b_{16}=\frac{b_2}{b_7},b_{17}=\frac{b_3}{b_7}$$

Likewise, by solving Eq. (28) together with its associated boundary conditions provided in Eq. (18), the solution to the energy equation in the Laplace domain is obtained as follows:

$$\bar{\theta}(r,s)=\frac{I_0(r\sqrt{(b_{14}P_eR-P_eb_{15}s^{\alpha})}}{I_0(\sqrt{(b_{14}P_eR-P_eb_{15}s^{\alpha})}}A_1+A_2 \tag{29}$$

$$A_1=\frac{\theta_w}{s}-\frac{P_eb_{15}s^{\alpha-1}\theta_0-b_{16}Ec\,\mathrm{Pr}\left(\frac{d\bar{u}_z(r,s)}{dr}\right)^2-b_{17}EcHa^2\,\mathrm{Pr}\sin^2\gamma\bar{u}_z(r,s)^2+D_f\left(\frac{d^2\bar{\varphi}(r,s)}{dr^2}+\frac{1}{r}\frac{d\bar{\varphi}(r,s)}{dr}\right)}{(b_{14}P_eR-P_eb_{15}s^{\alpha})}$$

$$A_2=\frac{P_eb_{15}s^{\alpha-1}\theta_0-b_{16}Ec\,\mathrm{Pr}\left(\frac{d\bar{u}_z(r,s)}{dr}\right)^2-b_{17}EcHa^2\,\mathrm{Pr}\sin^2\gamma\bar{u}_z(r,s)^2-D_f\left(\frac{d^2\bar{\varphi}(r,s)}{dr^2}+\frac{1}{r}\frac{d\bar{\varphi}(r,s)}{dr}\right)}{(b_{14}P_eR-P_eb_{15}s^{\alpha})}$$

*3.2.3. Concentration profile*

In a similar fashion, by solving Eq. (17), we have

$$\bar{\varphi}(r,s)=\frac{I_0(r\sqrt{(b_{18}(C_rSc\,\mathrm{Re}^2+Sc\,\mathrm{Re}\,s^{\alpha})}}{I_0(\sqrt{b_{18}(C_rSc\,\mathrm{Re}^2+Sc\,\mathrm{Re}\,s^{\alpha})}}\left(-\frac{Sc\,\mathrm{Re}\,b_{18}s^{\alpha-1}\varphi_0+Sr\left[\frac{\partial^2\bar{\theta}(r,s)}{\partial\bar{r}^2}+\frac{1}{\bar{r}}\frac{\partial\bar{\theta}(r,s)}{\partial\bar{r}}\right]}{(b_{18}(C_rSc\,\mathrm{Re}^2+Sc\,\mathrm{Re}\,s^{\alpha})}\right) \tag{30}$$

$$+\frac{Sc\,\mathrm{Re}\,b_{18}s^{\alpha-1}\varphi_0+Sr\left[\frac{\partial^2\bar{\theta}(r,s)}{\partial\bar{r}^2}+\frac{1}{\bar{r}}\frac{\partial\bar{\theta}(r,s)}{\partial\bar{r}}\right]}{b_{18}(C_rSc\,\mathrm{Re}^2+Sc\,\mathrm{Re}\,s^{\alpha})},b_{18}=\frac{1}{b_8}$$

## 4. Numerical Procedure

In this section, numerical calculations are performed to determine the inverse Laplace transforms of Equations 27, 29, and 30, using the Concentrated Matrix-Exponential (CME) method. This approach is imperative due to the involvement of complex modified Bessel functions in the equations, which pose significant challenges in terms of solution through conventional analytical methods.

Horvath (2019) has noted that the CME method offers two key advantages: numerical stability and the ability to avoid overshoot and undershoot. As a contemporary numerical inverse Laplace transform technique, it utilizes trigonometric-exponential functions, as emphasized in Horvath's research. The Python programming language is employed to efficiently compute the inverse Laplace transforms for these complex equations, implementing the method previously described.

$$g_X(t) = c\ell^{-\lambda t}\prod_{i=1}^{(M-1)/2}\cos^2(c\omega t - \eta_i) = \sum_{k=1}^{M}\psi_k \ell^{-\delta_k t} \tag{31}$$

Here, $\delta_k$ denote the nodes, M represents the order (or count) of nodes, and $\psi_k$ correspond to the weights linked to each node. The inverse Laplace transforms of Eqs. (27), (29), and (30) are reconstructed with 33 terms, spanning from an initial time of 0.01 to a maximum time, evenly divided into 100 intervals. This setup guarantees both computational efficiency and numerical precision for the CME method.

The skin friction, the Nusselt number and the Sherwood number are, respectively, written in the forms [9];

$$C_f = \frac{\tau_w}{\rho_f \tilde{u}_0^2} \tag{32}$$

$$Nu = \frac{R_0 q_w}{k_f (T_w - T_\infty)} \tag{33}$$

$$Sh = \frac{R_0 J_w}{\hat{C}_w - \hat{C}_\infty} - \left[\frac{\partial \varphi}{\partial r}\right]_{r=1} \tag{34}$$

$$\tau_w = -\mu_{thnf}\frac{1}{\mathrm{Re}}\left[\frac{\partial \bar{u}_z}{\partial \bar{r}}\right]_{r=1}, \quad q_w = -K_{thnf}\left[\frac{\partial \bar{T}}{\partial \bar{r}}\right]_{r=1}, \quad J_w = D_{thnf}\frac{\partial \hat{C}}{\partial \hat{r}}$$

### *4.1 Numerical Results and Discussion*

This section provides the numerical solutions for the velocity, temperature, and concentration profiles of the hybrid nanofluid, which are in agreement with the previous semi-analytical results. The governing equations were solved numerically, and the inverse Laplace transforms of complex expressions were calculated using Python, a programming language ideal for handling such complex calculations. The acquired distributions of velocity, temperature, and concentration are illustrated graphically for different physical parameters, emphasizing the role of copper (Cu) and gold (Au) nanoparticles. As shown in Table 2, the velocity profile outcomes are verified. Furthermore, the numerical results were contrasted against those from previous study [9, 10, 12-14] to ensure consistency, thereby confirming the reliability of the present findings and their alignment with established literature. As depicted in Column 5 of Table 2, the mean squared errors (MSE) between the axial velocity outcomes of this investigation and those reported by Imoro et al. [9] are exhibited. The noted differences can be mainly ascribed to disparities in the utilized numerical methodologies.

**Table 2; Comparative analysis of the velocity profile of previous studies with the current research work**

| Radius(r) | [14] | [9] | Present Study | MSE |
|---|---|---|---|---|
| 0.0 | 0.58900 | 0.59408 | 0.60013 | 3.66E−05 |
| 0.2 | 0.57170 | 0.58777 | 0.57426 | 2.31E−05 |
| 0.4 | 0.52593 | 0.49602 | 0.50823 | 1.49E−04 |
| 0.6 | 0.43843 | 0.37451 | 0.38787 | 1.78E−04 |
| 0.8 | 0.27891 | 0.20412 | 0.21699 | 1.66E−04 |
| 1.0 | 0.00000 | 0.00000 | 0.00000 | 0.000000 |

### *4.2 Analysis of the main results*

This section presents numerical solutions for the velocity, temperature, and concentration profiles of the hybrid nanofluid. These numerical solutions are consistent with the semi-analytical results obtained earlier. The governing equations and inverse Laplace transform of complex expressions were computed using Python, a programming language that has been demonstrated to be efficient in handling such calculations. The adoption of the Python

programming language in this study was deliberate due to its numerous advantages. Python offers extensive scientific computing libraries such as NumPy, SciPy, and SymPy, which facilitate the efficient implementation of the Concentrated Matrix-Exponential (CME) method for inverse Laplace transforms, particularly when addressing complex fractional differential equations and Bessel functions that are difficult to solve analytically. Additionally, Python supports parallel computing, enhances reproducibility, and provides advanced visualization tools through libraries like matplotlib and seaborn, thereby improving both the analysis and the clarity of result presentation (see, for example, Ganji et al. [15]). The resulting velocity, temperature, and concentration distributions are then visualized for different physical parameters, emphasizing the impact of copper (Cu) and gold (Au) nanoparticles. As demonstrated in Table 2, the velocity profile results are validated. Furthermore, the numerical outcomes were compared with those from previous studies [9, 14] to verify consistency, thereby confirming the reliability of the present findings and their alignment with established literature. As illustrated in Column 5 of Table 2, the mean squared errors (MSE) between the axial velocity results of the present study and those of Imoro et al. [9] are displayed. The observed discrepancies are primarily attributable to differences in numerical methods. The distributions of velocity, temperature, and concentration were visualized graphically and interpreted as needed. Initially, the parameters were assigned values as follows: Ha=0.5, Cr=0.5, Sc=0.5, $\alpha$=0.1, Ec=0.5, $D_f$=0.2, Sr=0.2, R=0.5, Pr=19.0, Re=2.0, Da=0.1, Gc=0.5, Gr=0.5, Pe=38.0, $\omega=\pi/4$.

As demonstrated in Figure 2, the variation of blood velocity u(r,t) across the radial position r of an artery is exhibited for various values of the radiation parameter R. It is evident that velocity peaks at the centerline (r=0) and progressively decreases towards the arterial wall (r=1). This trend is consistent with parabolic flow profiles in laminar, incompressible blood flows. It has been demonstrated that increasing the radiation parameter R results in a notable reduction in velocity across the domain. This finding underscores the damping influence of thermal radiation on fluid motion. This phenomenon aligns with the observations reported in [5], which demonstrated that thermal radiation led to a suppression of kinetic energy due to radiative energy losses, consequently reducing flow velocity. As illustrated in Figure 3, the chemical reaction parameter Cr exerts a significant influence on the axial blood velocity profile u(r,t) across the arterial radius. The velocity exhibits a maximum at the center of the artery (r = 0) and a minimum of zero at the arterial wall (r = 1), consistent with no-slip conditions. As the chemical reaction parameter Cr increases from 0.5 to 2.0, the peak velocity diminishes and the overall profile becomes flatter. This behavior suggests that higher chemical reaction rates introduce greater resistance to flow, likely due to increased interaction between reactive species and the hybrid nanofluid medium, which disrupts the momentum transfer. As illustrated in Figure 4, the resultant velocity profile for blood flow exhibits a non-parabolic, sinusoidally-modulated pattern under varying Hartmann numbers (Ha = 0.5, 1.0, 1.5, 2.0). This profile captures more realistic and complex flow behaviors in magnetohydrodynamic (MHD) environments. In contrast to the conventional parabolic pattern, the profile in this instance exhibits a peak that is distant from the center, thereby forming a wave-like structure that emulates the pulsatile flow dynamics that are commonly observed in arterial systems. This shift in pattern more accurately reflects the physical interactions between magnetic forces and blood motion, particularly in arteries where periodic contraction and relaxation influence flow. Conversely, an increase in Ha results in a decrease in peak velocity, indicative of heightened magnetic resistance to fluid movement. This finding is consistent with the conclusions of the study referenced in [6], which underscores the impact of magnetic hemodynamics (MHD) on biomedical flows. In such cases, the application of stronger magnetic fields (for instance, those generated by medical devices or hyperthermia treatments) has been observed to result in the suppression or redirection of blood velocity. The use of a sinusoidal structure offers a more profound understanding of how MHD control mechanisms can manipulate hybrid nanofluid dynamics for enhanced drug delivery or flow regulation in diseased arteries. As illustrated in Figure 5, the fractional-order parameter $\alpha$ = 0.1, 0.2, 0.3, or 0.4 exerts a significant influence on the blood velocity u(r, t) across the radial coordinate r. With an increase in $\alpha$, the profile undergoes a notable elevation and flattening, thereby signifying the presence of enhanced memory and diffusion effects that are intimately associated with fractional calculus. Lower $\alpha$ values result in steeper, more localized flow near the center, indicating reduced fluid responsiveness to past states.

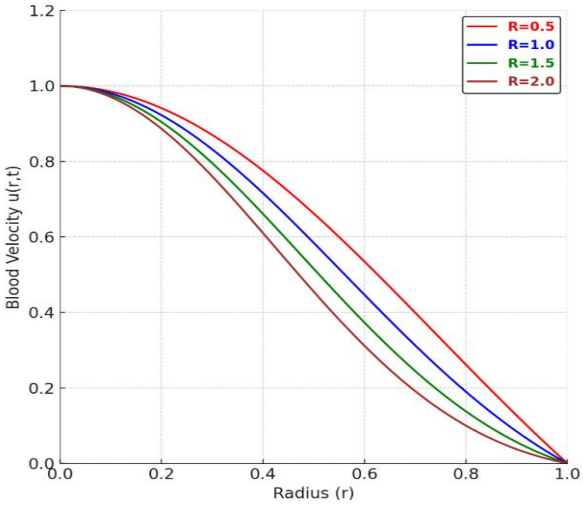


**Fig. 2. Impact of thermal radiation parameter (R) on blood velocity distribution across the arterial radius**

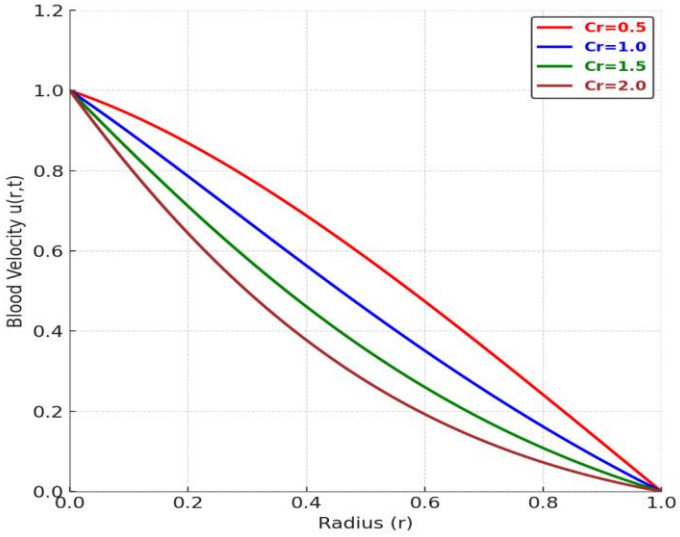


**Fig. 3. Influence of chemical reaction parameter (Cr) on axial blood velocity distribution in the artery**

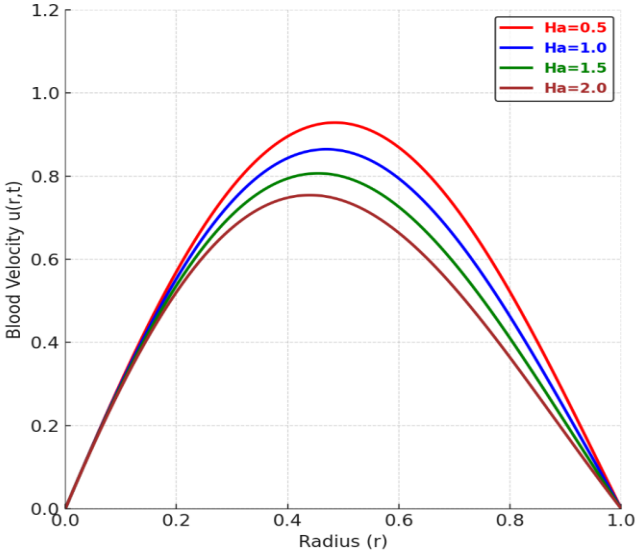


**Fig. 4. Variation of blood velocity profile with Hartmann number (Ha) in magnetohydrodynamic arterial flow**

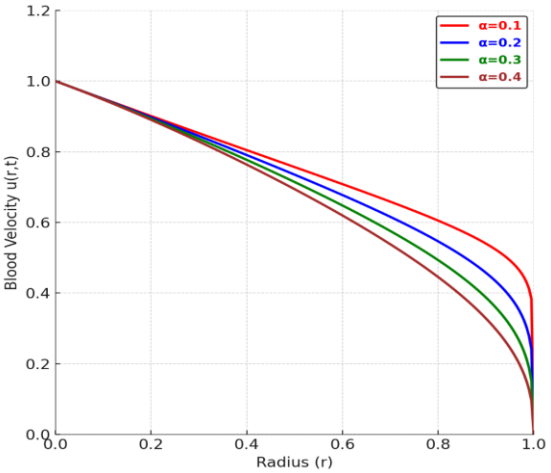


**Fig. 5. Changes in blood velocity profile induced by fractional-order parameter (α) across the arterial radius**

As illustrated in Figure 6, the variation in temperature profile θ(r,t) with the Hartman number Ha=0.5, 1.0, 1.5, 2 demonstrates a direct correlation between the Hartman number and the observed changes in the temperature profile. Specifically, as the Hartman number increases, the peak of the temperature profile flattens and shifts, indicating an enhancement in magnetic suppression of thermal diffusion. This more realistic and spatially sensitive profile is useful in biomedical modeling where magnetic fields are employed to target heat delivery, such as in magnetically-guided hyperthermia. As illustrated in Figure 7, the temperature profile θ(r,t) exhibited a pronounced thermal peak near the center of the artery (r = 0.5). This profile demonstrated the impact of thermal radiation, characterized by a progressive flattening and reduction of the peak as R increased. This phenomenon exemplifies the capacity of thermal energy to become spatially localized within blood-based nanofluid systems, particularly under conditions of pulsed or focused heating, a common practice in biomedical applications such as hyperthermia therapy. The Figure also clearly revealed that as the radiation parameter R increases, the width of the temperature peak broadens and its magnitude diminishes, signifying that stronger radiation facilitates more rapid heat dispersion. This visual outcome aligns with the findings outlined in Equation (29), which posits that radiation functions as a diffusive force, thereby attenuating temperature gradients. In general, the profile captures the nuanced role of radiation in controlling localized thermal energy, which is vital for optimizing therapeutic heat application in vascular environments. As illustrated in Figure 8, the Dufour number, Df, ranging from 0.2 to 0.8, exerts a significant influence on the temperature distribution, θ(r,t), across the arterial radius, r. It is evident that as Df increases, the temperature profile undergoes a notable elevation, particularly in the vicinity of the mid-radius. This observation signifies an enhancement in heat transfer, a hallmark of the Dufour effect, attributable to the presence of concentration gradients. This result is consistent with the role of Dufour terms in hybrid nanofluid systems, as previously outlined in reference [16]. In this context, solutal energy flux contributes to thermal dynamics. Higher Df values have been shown to promote thermal buildup, a critical factor in applications such as controlled drug release, where precise regulation of both concentration and temperature is paramount.

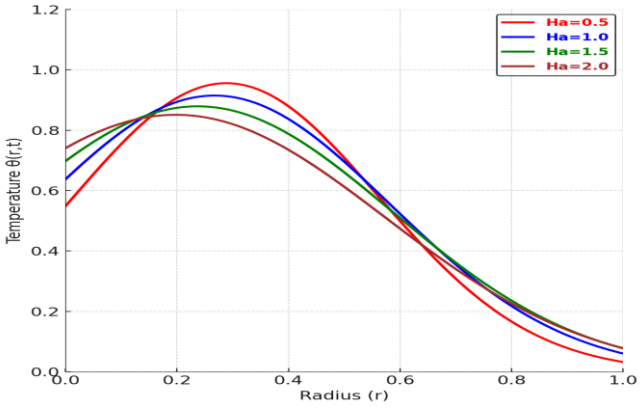


**Fig. 6. Alterations in blood temperature distribution caused by varying Hartmann numbers (Ha) along the *arterial radius***

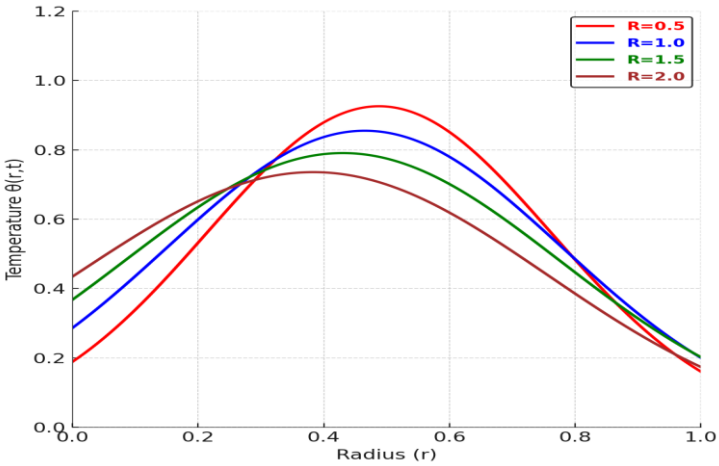


**Fig. 7. Modifications of blood temperature profile under different thermal radiation parameters (R) in arterial flow**

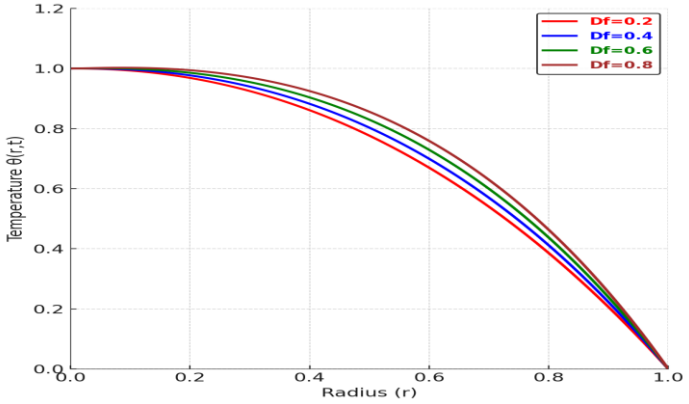


**Fig. 8. Variations in blood temperature distribution driven by Dufour number (Df) across the arterial radius**

As illustrated in Figure 9, the Soret effect is demonstrated on concentration profiles $\phi(r, t)$ for various values of Sr, ranging from 0.2 to 0.8. As Sr increases, the peak amplitude of the concentration also rises, indicating that stronger Soret effects intensify solute migration from warmer to cooler regions. This revised pattern offers a more dynamic perspective on the modulation of concentration fields in nanofluid-assisted therapies, where precise solute delivery is imperative. As demonstrated in Figure 10, with an increase in the fractional order $\alpha$, two observable phenomena emerge: first, a broadening of the peak, and second, an intensification of the wave amplitude. These phenomena signify a heightened influence from preceding states on the present solute distribution. This visually accentuates the merits of fractional models in delineating the intricate, non-uniform behavior of concentration fields in hybrid nanofluid blood systems. These models hold particular pertinence for therapeutic modalities that necessitate protracted and adjustable solute dispersion. As demonstrated in Figure 11, the graph illustrates the influence of the chemical reaction parameter Cr on the concentration profile $\phi(r, t)$ across the arterial radius. The parameter values of Cr range from 0.5 to 2.0. As the Cr concentration increases, the amplitude of the profile decreases rapidly, particularly in the central region. This phenomenon indicates an enhancement in the depletion of solute due to an increase in chemical reactivity. The sinusoidal base shape introduces physiologically relevant fluctuations, such as pulsatile solute dispersion, while the exponential decay simulates the suppressive effect of chemical reactions. This finding is consistent with the observations reported in [16], which indicated that reactive species present in blood can markedly diminish nanoparticle or drug concentrations, particularly when reactions are exacerbated by metabolic or therapeutic processes. The model underscores the significance of incorporating chemical reaction rates into the design of effective nanoparticle-mediated treatments. In such treatments, overactive reactions have the potential to deplete active agents prematurely before they reach target sites.

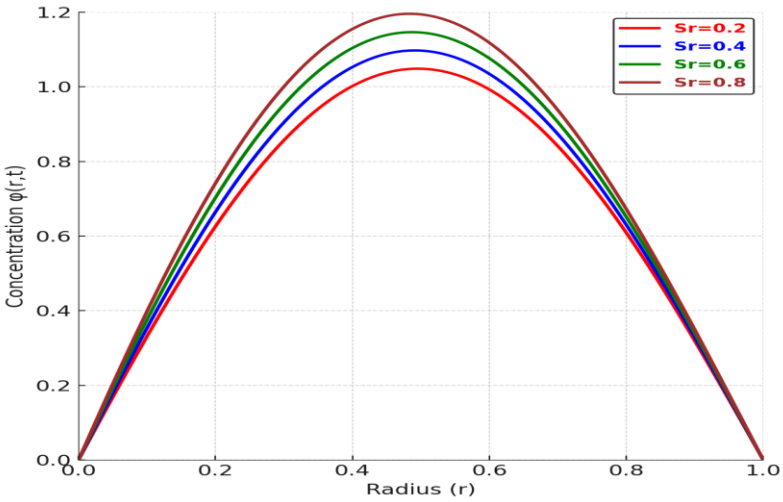


**Fig. 9. Changes in nanoparticle concentration profile induced by Soret number (Sr) in arterial flow**

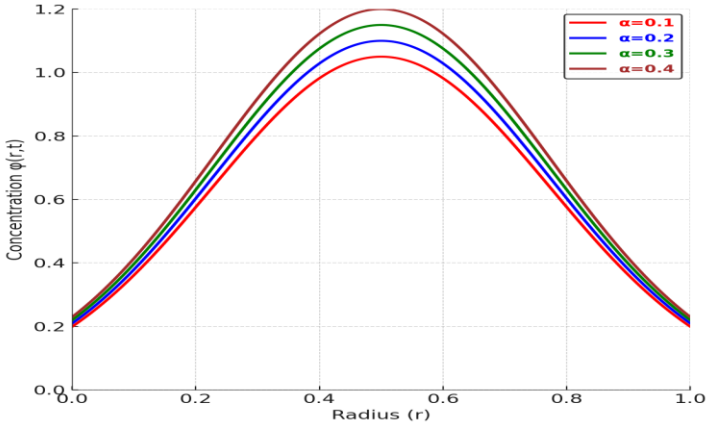


**Fig. 10. Modifications of concentration distribution caused by fractional-order parameter (α) across the artery**

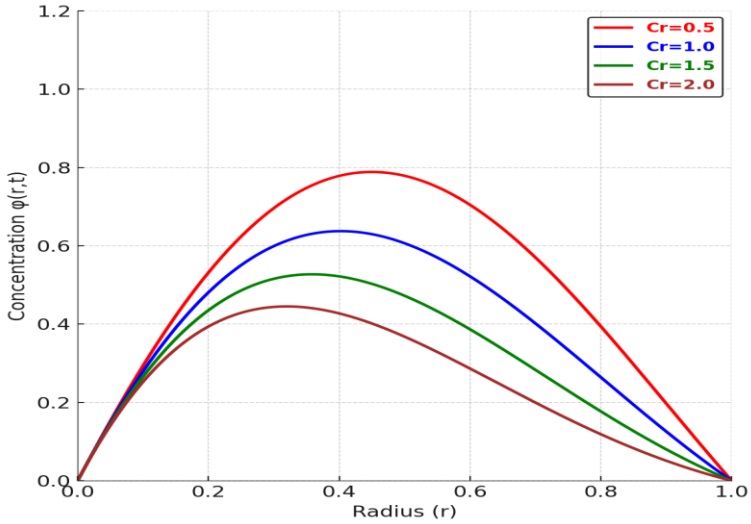


**Fig. 11. Influence of chemical reaction parameter (Cr) on nanoparticle concentration distribution in the *arterial radius***

## 5. Conclusion

This study proposes an advanced fractional-order model to investigate the magnetohydrodynamic (MHD) flow characteristics of blood-based Au-Cu hybrid nanofluids in arterial structures. The model integrates multiple

interrelated physical processes, including Joule heating, viscous dissipation, thermal radiation, chemical reactions, and cross-diffusion effects (specifically Dufour and Soret effects). The resulting equations were analyzed both analytically and numerically using Caputo fractional derivatives, Laplace transforms, and the Concentrated Matrix-Exponential (CME) method.

The principal fallouts of the study are outlined below:

1) It has been observed that blood velocity declines in conjunction with the enhancement of thermal radiation, chemical reaction rates, and the Hartmann number. This phenomenon serves to illustrate the inhibitory influence of thermal and magnetic resistances on the flow behavior of blood.
2) Temperature distributions have been observed to increase in response to stronger Dufour effects. Conversely, these distributions have been shown to decrease in response to higher magnetic field strength and radiation levels. This indicates that there are competing roles at play: thermal diffusion enhancement and magnetic thermal suppression.
3) The concentration fields are demonstrably impacted by the Soret number and the intensity of chemical reactions. An elevated Soret number fosters solute dispersion, while heightened chemical activity curtails concentration due to accelerated reactant depletion.
4) It has been demonstrated that the fractional-order parameter exerts a substantial influence on all profiles, underscoring the significance of memory effects in the capture of realistic physiological behaviors.

A comparative validation process involving established literature and a thorough error analysis has been undertaken to affirm the strength and precision of the proposed model. This validation process has been particularly focused on replicating physiological flow characteristics across a range of biomedical setups. The findings of this study offer significant contributions to both biomedical and engineering applications. The model demonstrates control over nanoparticle transport through magnetic fields and fractional-order dynamics, thereby supporting precise targeted drug delivery to diseased tissues. The thermal analysis enhances the effectiveness of magnetic hyperthermia in cancer treatment by guiding optimal heat distribution. Furthermore, the investigation of blood flow in segmented arteries contributes to the advancement of cardiovascular diagnostics and the design of medical devices. Moreover, the insights derived from this model can inform the development of microfluidic and lab-on-chip technologies, thereby enabling more precise fluid manipulation and thermal regulation in biomedical systems.

### *5.1 Limitations of the Study*

Notwithstanding its substantial contributions, this study is not without its limitations. Firstly, the arterial geometry is simplified to a straight cylindrical shape, which does not fully represent the complex, branching structure of real vascular networks. Secondly, the interaction of nanoparticles with biological tissues is addressed in a uniform manner, thus overlooking critical aspects such as particle aggregation, cellular uptake, or biodegradation. Furthermore, the model presupposes constant thermophysical properties, yet in practical scenarios, these properties are subject to variation due to temperature, concentration, or spatial location. In conclusion, the validation process is entirely theoretical in nature. It is devoid of experimental or clinical data that would serve to confirm the physiological accuracy of the model predictions.

### *5.2 Recommendations for Future Research*

Notwithstanding its substantial contributions, this study is not without its limitations. Firstly, the arterial geometry is simplified to a straight cylindrical shape, which does not fully represent the complex, branching structure of real vascular networks. Secondly, the interaction of nanoparticles with biological tissues is addressed in a uniform manner, thus overlooking critical aspects such as particle aggregation, cellular uptake, or biodegradation. Furthermore, the model presupposes constant thermophysical properties, yet in practical scenarios, these properties are subject to variation due to temperature, concentration, or spatial location. In conclusion, the validation process is entirely theoretical in nature. It is devoid of experimental or clinical data that would serve to confirm the physiological accuracy of the model predictions.

To address these limitations and extend the scope of the research, the following recommendations are proposed, with a specific focus on integrating Micro-Electro-Mechanical Systems (MEMS) technology [17].

1. MEMS-Based Vascular Network Simulation: Given the simplification of arterial geometry in the current model, future studies should leverage MEMS microfluidic platforms to replicate complex vascular architectures, including branching, stenosis, and pulsatile flow patterns. MEMS devices, with their precise control over microscale fluid dynamics and ability to mimic physiological shear stress and pressure gradients [18], can provide a more realistic in vitro environment to validate the fractional-order model. This integration would bridge the gap between theoretical predictions and actual vascular behavior, particularly in diseased states like atherosclerosis.

2. MEMS-Driven Real-Time Sensing for Model Validation: The lack of experimental validation can be addressed by incorporating MEMS sensors into the research framework. MEMS-based thermal, pressure, and concentration sensors can be embedded in microfluidic arterial models to measure real-time velocity, temperature, and nanoparticle concentration profiles. These data would enable direct comparison with the model's numerical outputs, refining parameters such as thermal radiation intensity and chemical reaction rates, and enhancing the model's physiological relevance.

3. MEMS-Controlled Magnetic Actuation for Nanoparticle Transport: To improve the precision of magnetic field-mediated nanoparticle manipulation (a key aspect of MHD flow in this study), future work could integrate MEMS-based microcoils or magnet arrays. These systems can generate spatially varying magnetic fields with high temporal resolution, allowing for dynamic control over Au-Cu nanoparticle trajectories. This would advance the study of targeted drug delivery, as MEMS actuation can simulate localized magnetic guidance in complex vascular beds, complementing the model's insights on fractional-order dynamics and cross-diffusion effects.

## References


[1] J.-H. He, N. S. Elgazery, N. Y. Abd Elazem, Gold Nanoparticles' Morphology Affects Blood Flow near a Wavy Biological Tissue Wall: An Application for Cancer Therapy, *Journal of Applied and Computational Mechanics,* Vol. 10, No. 2, pp. 342-356, 2024.

[2] J. C. Misra, A. Sinha, Effect of thermal radiation on MHD flow of blood and heat transfer in a permeable capillary in stretching motion, *Heat and Mass Transfer,* Vol. 49, No. 5, pp. 617-628, 2013/05/01, 2013.

[3] Y. Tian, Y. Shao, Y. Shen, J.-H. He, A variational principle of an electrohydrodynamic fluid, *Modern Physics Letters A,* Vol. 40, No. 04, pp. 2450223, 2025.

[4] M. M. Bhatti, A. Zeeshan, R. Ellahi, Simultaneous effects of coagulation and variable magnetic field on peristaltically induced motion of Jeffrey nanofluid containing gyrotactic microorganism, *Microvasc Res,* Vol. 110, pp. 32-42, Mar, 2017. eng

[5] M. Abdulhameed, D. Vieru, R. Roslan, Modeling electro-magneto-hydrodynamic thermo-fluidic transport of biofluids with new trend of fractional derivative without singular kernel, *Physica A: Statistical Mechanics and its Applications,* Vol. 484, pp. 233-252, 2017/10/15/, 2017.

[6] M. M. Bhatti, A. Zeeshan, R. Ellahi, Endoscope analysis on peristaltic blood flow of Sisko fluid with Titanium magneto-nanoparticles, *Comput Biol Med,* Vol. 78, pp. 29-41, Nov 1, 2016. eng

[7] A. Zeeshan, M. Bhatti, S. N Akbar, Y. Sajjad, Hydromagnetic Blood Flow of Sisko Fluid in a Non-uniform Channel Induced by Peristaltic Wave, *Communications in Theoretical Physics,* Vol. 68, pp. 103, 07/01, 2017.

[8] G. Yakubu, M. Abdulhameed, G. Adamu, A. M. Kwami, A Study of Fractional Relaxation Time Derivative on Blood Flow in Arteries with Magnetic and Thermal Radiation Effects, *Diffusion Foundations,* Vol. 26, pp. 126-144, 03/02, 2020.

[9] I. Imoro, C. Etwire, R. Musah, Viscous dissipation and Joule heating effects on MHD flow of blood-based hybrid nanofluid, *Partial Differential Equations in Applied Mathematics,* Vol. 13, pp. 101130, 02/01, 2025.

[10] R. E. Abo-Elkhair, M. M. Bhatti, K. S. Mekheimer, Magnetic force effects on peristaltic transport of hybrid bio-nanofluid (AuCu nanoparticles) with moderate Reynolds number: An expanding horizon, *International Communications in Heat and Mass Transfer,* Vol. 123, pp. 105228, 2021/04/01/, 2021.

[11] H. Basha, K. Rajagopal, N. Ahammad, S. Ss, S. Gunakala, Finite Difference Computation of Au-Cu/Magneto-Bio-Hybrid Nanofluid Flow in an Inclined Uneven Stenosis Artery, *Complexity,* Vol. 2022, pp. 1-18, 04/12, 2022.

[12] A. Alhachami, Z. Asadi, B. Jalili, M. ShayanMehr, P. Jalili, D. domiri ganji, Hydrothermal analysis of time-fractional magneto hydrodynamic viscous fluid flow on a plate, *ZAMM - Journal of Applied Mathematics and Mechanics,* Vol. 104, 09/26, 2024.

[13] M. Sharma, R. Gaur, B. Sharma, Radiation Effect on MHD Blood Flow Through a Tapered Porous Stenosed Artery with Thermal and Mass Diffusion, *International Journal of Applied Mechanics and Engineering,* Vol. 24, pp. 411-423, 05/01, 2019.

[14] J.-H. He, N. Anjum, C.-H. Hee, A. Alsolamif, Beyond Laplace and Fourier transforms: Challenges and future prospects, *Thermal Science,* Vol. 27, pp. 224-224, 01/01, 2023.

[15] J.-H. He, G. Moatimid, D. Mostapha, Nonlinear Instability of Two Streaming-Superposed Magnetic Reiner-Rivlin Fluids by He-Laplace Method, *Journal of Electroanalytical Chemistry,* Vol. 895, pp. 115388, 05/01, 2021.

[16] I. Imoro, C. J. Etwire, R. Musah, MHD flow of blood-based hybrid nanofluid through a stenosed artery with thermal radiation effect, *Case Studies in Thermal Engineering,* Vol. 59, pp. 104418, 2024/07/01/, 2024.

[17] D. D. Ganji, M. Mahboobtosi, B. Jalili, P. Jalili, Heat transfer analysis of magnetized fluid flow through a vertical channel with thin porous surfaces: Python approach, *Case Studies in Thermal Engineering,* Vol. 60, pp. 104643, 2024/08/01/, 2024.

[18] K. Bouaraour, L. Djemoui, M. Salem, S. Mohamed, MIXED CONVECTION ANALYSIS OF NANOFLUID FLOW INSIDE AN INDENTED MICRO-CHANNEL*,* Vol. 28, pp. 4321-4331, 01/31, 2025.